Primordial black holes generated by fast-roll mechanism in non-canonical natural inflation

Soma Heydari* and Kayoomars Karami[†]

Department of Physics, University of Kurdistan,

Pasdaran Street, P.O. Box 66177-15175, Sanandaj, Iran

(Dated: May 15, 2024)

Abstract

In this work, a new fast-roll (FR) mechanism to generate primordial black holes (PBHs) and their coeval gravitational waves (GWs) in generalized non-canonical natural inflation is introduced. In this model, choosing a suitable function for non-canonical mass scale parameter $M(\phi)$ gives rise to produce a cliff-like region in field evolution path. When inflaton rolls down the steep cliff, its kinetic energy during the FR stage is amplified in comparison with slow-roll (SR) stage. Hence, seeds of PBHs production are born in this transient FR stage. Depending on the position of the cliff, appropriate cases of PBHs for explaining total dark matter (DM), microlensing effects, LIGO-VIRGO events and NANOGrav 15 year data can be formed. The density spectrum of GWs related to one case of the model lies in the NANOGrav 15 year domain and behaves like $\Omega_{\rm GW_0} \sim f^{5-\gamma}$. The spectral index $\gamma = 3.42$ for this case satisfies the NANOGrav 15 year constraint. Moreover, regarding reheating considerations, it is demonstrated that PBHs are born in radiation-dominated (RD) era. Furthermore, viability of the model in light of theoretical swampland criteria and observational constraints on cosmic microwave background (CMB) scales are illustrated.

PACS numbers:

^{*} s.heydari@uok.ac.ir

[†] kkarami@uok.ac.ir

I. INTRODUCTION

Recently, primordial black holes (PBHs) as remarkable candidate for cosmological budget of dark matter (DM) have attracted a lot of interests from scientific community [1-41]. PBHs with masses around $10M_{\odot}$ (M_{\odot} expresses the solar mass) also could be considered as possible source of ferreted out gravitational waves (GWs) by LIGO-Virgo teamwork [42–46]. Into the bargain, lighter PBHs with masses around the earth mass could be used to explain microlensing events in OGLE data [47, 48]. Lately, pulsar timing array EPTA, PPTA and CPTA as well as NANOGrav teamwork have succeed to trace low-frequency GWs [49–58]. Interestingly enough, the emitted GWs from PBHs formation could be contemplated as promising origin of the NANOGrav signals [59–65]. Moreover, PBHs are likely candidate for formation of super-massive black holes in the center of galaxies [66–69]. Generally, PBHs are born from sizable density fluctuations, when they return to horizon in radiation-dominated (RD) era. These fluctuations are originated from scalar fluctuations produced in inflation epoch. Basically, in order to produce seeds of PBHs in the inflationary epoch, it is required to have a proper mechanism for enhancing the power spectrum of scalar perturbations to $\mathcal{P}_{\mathcal{R}} \sim \mathcal{O}(10^{-2})$ on small scales with respect to that on cosmic microwave background (CMB) scale.

Mostly, PBHs models include an inflationary epoch composed of three sequential stages so called, first slow-roll (SR) stage, intermediate ultra-slow-roll (USR) stage and final SR stage. Usually, in the first SR stage, CMB anisotropies are produced and leave the horizon. In this stage, the first and second SR parameters (ε_1 and ε_2) are very smaller than one to guarantee the SR conditions { ε_1 , ε_2 } $\ll 1$. When the inflaton gets the USR stage, owing to high friction, it decelerates and its kinetic energy decreases in comparison with SR stage. Also, severe reduction in the ε_1 value takes place and simultaneously, the ε_2 parameter after reaching a large negative value takes large positive values higher than one. So, the SR condition is violated by ε_2 in the USR stage and subsequent to that amplitude of the $\mathcal{P}_{\mathcal{R}}$ amplifies to $\mathcal{O}(10^{-2})$, which is essential to produce PBHs [3–15, 23–26]. After the USR stage, the inflaton enters the final SR stage which realizes the end of inflation. In this final stage, the values of ε_1 , ε_2 and kinetic energy of the inflaton almost return to their values in the first SR stage. But the USR mechanism is not the only case for PBHs generation. In recent years, some inflationary models to explain PBHs generation have been introduced, which

containing special form of potentials in the presence of a downward step like a cliff on small scale far from the CMB scale [70, 71]. In these works, it is demonstrated that, amplification of the scalar power spectrum to around 7 order of greatness through a transient fast-roll (FR) mechanism during the stage of cliff passing is possible. In these models, inflationary era composed of the first SR stage to produce CMB anistropies, the intermediate FR stage to born PBHs and the final SR to end of the inflation. In the FR stage, the inflaton experiences increase in its speed, kinetic energy and value of ε_1 parameter. Same as the USR stage, the SR condition in the FR stage is violated via the ε_2 parameter. In fact, particle production as a result of non-adiabatic transition between SR and FR stage in the cliff position, gives rise to perturbation magnification and born PBHs seeds. Hitherto, FR mechanism is established in canonical standard model of inflation through altering the potential to realize a cliff-like region in the path of field evolution [70, 71].

It is known that, one of the successful generalization of the standard model of inflation to revive the steep potentials and produce PBHs and GWs is power-law non-canonical (PLNC) model containing Lagrangian $\mathcal{L}(X,\phi) = X^{\alpha} - V(\phi)$ (X expresses canonical kinetic energy) [2–4, 72–77]. It is obvious that, diversion of the canonical standard inflationary model is defined by $\alpha > 1$ ($\alpha = 1$ corresponds to canonical Lagrangian). In [3], PBHs and GWs formation from the quartic potential in generalized power-law non-canonical (GPLNC) inflationary model have been investigated. In the GPLNC setup, non-canonical mass scale parameter $M(\phi)$ is chosen as a general function of scalar field rather than being constant as in the PLNC model.

The aim of this study is probing generation of PBHs and their coeval GWs from natural potential in the GPLNC setup through FR mechanism. It is tried to utilize the dependency of M to the scalar field to produce a FR span on a cliff in the field evolution pass to generate PBHs. Using the reheating consideration, we attempt to show that PBHs are born in the RD era. To this end, in Sec. II, a brief review of GPLNC model is presented. In Sec. III, feasibility of the model theoretically and observationally is checked and used method to produce PBHs is explained. In Sec. IV, reheating computation is described. Thence, spectra of PBHs mass in Sec. V and coeval GWs with PBHs in Sec. VI are elucidated. Lastly, Sec. VII is earmarked as conclusions of the work.

II. REVIEW OF THE GPLNC MODEL

A. Background evolution

This section is started with the ensuing action

$$S = \int d^4x \sqrt{-g} \left[M_P^2 \frac{R}{2} + \mathcal{L}(X, \phi) \right], \tag{1}$$

therein, g, $M_P = 1/\sqrt{8\pi G}$, R and $\mathcal{L}(X,\phi)$ are respectively, determinant of the metric tensor $g_{\mu\nu}$, reduced Planck mass, Ricci scalar and Lagrangian density. Regarding the generality of the Lagrangian density function to the scalar field ϕ and kinetic energy $X \equiv \frac{1}{2}g_{\mu\nu}\partial^{\mu}\phi\partial^{\nu}\phi$ [2–4, 72–77], we are interested in the GPLNC form of that as [3]

$$\mathcal{L}(X,\phi) = X \left(\frac{X}{M^4(\phi)}\right)^{\alpha-1} - V(\phi), \tag{2}$$

wherein, α with no dimension defines diversion from canonicity. It means that, if $\alpha = 1$, the Lagrangian (2) regains its canonical form. The non-canonical mass scale parameter $M(\phi)$ with mass dimension could be specified as a generic function of the scalar field ϕ . It is notable that, the conventional form of the Lagrangian of the PLNC model with constant M could be recovered through a suitable field redefinition for the Lagrangian (2) [3]. Furthermore, the inflationary potential is denoted by $V(\phi)$ in the Lagrangian (2). In the following, utilizing the Lagrangian density (2), one can compute energy density ρ_{ϕ} and pressure p_{ϕ} for the scalar field as

$$\rho_{\phi} = 2X\mathcal{L}_{,X} - \mathcal{L} = (2\alpha - 1)X\left(\frac{X}{M^{4}(\phi)}\right)^{\alpha - 1} + V(\phi), \tag{3}$$

$$p_{\phi} = \mathcal{L} = X \left(\frac{X}{M^4(\phi)} \right)^{\alpha - 1} - V(\phi), \tag{4}$$

where, (,x) means partial derivative versus X. Homogeneity and isotropy of the universe are expressed via the flat Friedmann-Robertson-Walker (FRW) metric as $g_{\mu\nu} = \operatorname{diag}\left(1, -a^2(t), -a^2(t), -a^2(t)\right)$, wherein a(t) indicates scale factor as a function of cosmic time t. Taking variation of the action (1) against the metric $g_{\mu\nu}$ results in the Friedmann equations as

$$H^{2} = \frac{\rho_{\phi}}{3M_{P}^{2}} = \frac{1}{3M_{P}^{2}} \left[(2\alpha - 1) X \left(\frac{X}{M^{4}(\phi)} \right)^{\alpha - 1} + V(\phi) \right], \tag{5}$$

$$\dot{H} = \frac{-(\rho_{\phi} + p_{\phi})}{2M_P^2} = -\frac{\alpha}{M_P^2} X \left(\frac{X}{M^4(\phi)}\right)^{\alpha - 1},$$
 (6)

therein $H \equiv \dot{a}/a$ signifies the Hubble parameter (dot means derivative versus t). Likewise, taking variation of the action (1) against the scalar field ϕ results in field evolution equation as

$$\ddot{\phi} + \frac{3H\dot{\phi}}{2\alpha - 1} - 2\left(1 - \frac{1}{\alpha}\right) \left(\frac{M_{,\phi}}{M(\phi)}\right) \dot{\phi}^2 + \frac{1}{\alpha} \left(\frac{V_{,\phi}}{2\alpha - 1}\right) \left(\frac{2M^4(\phi)}{\dot{\phi}^2}\right)^{\alpha - 1} = 0,\tag{7}$$

in which $(,\phi)$ means derivative versus ϕ . Thenceforth, the 1st and 2nd Hubble SR parameters are given by

$$\varepsilon_1 \equiv -\frac{\dot{H}}{H^2}, \quad \varepsilon_2 \equiv \frac{\dot{\varepsilon_1}}{H \,\varepsilon_1}.$$
(8)

In the SR domain $\{\varepsilon_1, \varepsilon_2\} \ll 1$, potential energy prevails the kinetic energy. It is notable that, conflation of Eqs. (5)-(7) and utilizing the 1st SR parameter beside e-folds number definition dN = Hdt, the equation of field evolution (7) is rewritten as ensuing form

$$\phi_{,NN} + \left[\frac{V_{,\phi}}{2V\varepsilon_1} \left(\frac{3}{2\alpha - 1} - \frac{\varepsilon_1}{\alpha} \right) - \frac{2M_{,\phi}}{M(\phi)} \left(1 - \frac{1}{\alpha} \right) \right] \phi_{,N}^2 + \left[\frac{3}{2\alpha - 1} - \varepsilon_1 \right] \phi_{,N} = 0, \quad (9)$$

therein (N) and (N) designate the 1st and 2nd derivative versus e-folds number N.

B. Evolutions of scalar and tensor perturbations

Subsequent to analyses of [73, 78] in NC setup, the evolutions of the scalar and tensor perturbations are governed by Mukhanonv-Sasaki (MS) equations, which are derived from expanding the action (1) to second order in perturbations. In this framework, the MS equation for the curvature \mathcal{R} perturbations is given by

$$u_k'' + \left(c_s^2 k^2 - \frac{z''}{z}\right) u_k = 0, \tag{10}$$

where, (') means derivative versus conformal time $\eta \equiv \int dt/a(t)$ and

$$u_k \equiv z \mathcal{R}_k, \qquad z \equiv \frac{a\sqrt{\rho_\phi + p_\phi}}{c_s H}, \qquad c_s^2 \equiv \frac{\mathcal{L}_{,X}}{2X\mathcal{L}_{,XX} + \mathcal{L}_{,X}}.$$
 (11)

Thus, the power spectrum of the curvature perturbations is acquired from the solution of MS equation (10) as

$$\mathcal{P}_{\mathcal{R}} \equiv \frac{k^3}{2\pi^2} \left| \frac{u_k^2}{z^2} \right|. \tag{12}$$

In the SR domain when the comoving wavenumber k crosses the sound horizon $(c_s k = aH)$, the $\mathcal{P}_{\mathcal{R}}$ is approximated as [78]

$$\mathcal{P}_{\mathcal{R}} = \frac{H^2}{8\pi^2 M_P^2 c_s \varepsilon_1} \Big|_{c_s k = aH}.$$
 (13)

The observational restriction on the curvature power spectrum at pivot scale ($k_* = 0.05 \text{ Mpc}^{-1}$) enforced by Planck collaboration is $\mathcal{P}_{\mathcal{R}}(k_*) \simeq 2.1 \times 10^{-9}$ [79]. Regarding the Lagrangian (2), the c_s in our setup is obtained as

$$c_s = (2\alpha - 1)^{-1/2}. (14)$$

So as to preclude the model from classical instability, it is essential to have $0 < c_s^2 \le 1$ which leads to a lower bound on the α parameter as $\alpha \ge 1$. Moreover, using the curvature power spectrum (13), the scalar spectral index n_s can be derived with respect to SR parameters as

$$n_s - 1 \equiv \frac{d \ln \mathcal{P}_{\mathcal{R}}}{d \ln k} \simeq -2\varepsilon_1 - \varepsilon_2.$$
 (15)

The observational bound on the scalar spectral index through the recent data of Planck 2018 is $n_s = 0.9649 \pm 0.0042$ (TT, TE, EE+lowE+lensing+BK18+BAO, 68% CL) [79].

Likewise, the MS equation governing the tensor perturbations in this setup is given by

$$v_k'' + \left(k^2 - \frac{a''}{a}\right)v_k = 0, (16)$$

wherein, $v_k \equiv ah_k$, So, the power spectrum of tensor perturbations is calculated from the solution of the tensor MS equation (16) as follows

$$\mathcal{P}_t \equiv \frac{k^3}{\pi^2} \left| \frac{{\upsilon_k}^2}{a^2} \right|,\tag{17}$$

which, in the SR domain at k = aH, is approximated as [78]

$$\mathcal{P}_t = \frac{2H^2}{\pi^2 M_D^2} \bigg|_{k=aH}.$$
(18)

The tensor-to-scalar ratio r in terms of the 1st SR parameter is attained from (13) and (18) as

$$r \equiv \frac{\mathcal{P}_t}{\mathcal{P}_{\mathcal{P}}} \simeq 16c_s \varepsilon_1. \tag{19}$$

The recent upper limit on the r, established by Planck and BICEP/Keck 2018 data, is r < 0.036 (TT, TE, EE +LowE +Lensing +BK18+BAO, 95% CL) [80].

III. FAST-ROLL MECHANISM AND FEASIBILITY OF THE MODEL

The aim of this section is showing that, using the FR mechanism in the GPLNC model, the required enhancement in the curvature power spectrum to produce PBHs seeds can occur. At the same time, this enhancement on small scales should not ruin the feasibility of the model on CMB scale in light of theoretical and observational constraints. Therefore, the non-canonical mass scale parameter $M(\phi)$ for the Lagrangian (2) is defined as a twofold function of ϕ as follows

$$M(\phi) = M_0 \Big[1 + \epsilon(\phi) \Big], \tag{20}$$

where

$$\epsilon(\phi) = \omega \cosh^{-2} \left(\frac{\phi - \phi_c}{b} \right). \tag{21}$$

In the 1st part of Eq. (20), the parameter M_0 with mass dimension, affects the consistency of the model with CMB data on large scales. In the second part, the dimensionless function $\epsilon(\phi)$ is employed to produce a local steep cliff in the field evolution path. For this purpose, a piked function like Eq. (21) is selected for $\epsilon(\phi)$, which illustrates a local peak at $\phi = \phi_c$ with width b and elevation ω . Here, ϕ_c and b have mass dimensions whereas ω is dimensionless. From Eq. (21), it is obvious that the piked function $\epsilon(\phi)$ for $\phi \neq \phi_c$ gradually dies out $\epsilon(\phi) \ll 1$. Thus, $M(\phi)$ in GPLNC setup reverts to constant M_0 in the conventional PLNC setup. The function $\epsilon(\phi)$ in GPLNC framework, has the ability to produce a local steep cliff in $\phi = \phi_c$ with altitude of b on the field evolution path. When the inflaton reaches the cliff position, rolls down faster and its kinetic energy enhances in comparison with SR domain (see plots of Fig. 1). Hence, a transient FR stage is produced in the proximity of $\phi = \phi_c$ and subsequent to that the curvature power spectrum enhances to required value for generating PBHs seeds. In fact, a non-adiabatic transition from the SR stage to FR stage gives rise to particle production and enhance the scalar perturbation to produce PBHs. Therefore, it is necessary to regulate three parameters $\{\omega, \phi_c, b\}$ of the $\epsilon(\phi)$ function to have a suitable FR stage to generate PBHs seeds on small scales.

In the following, natural inflationary potential is chosen for the model

$$V(\phi) = \Lambda^4 \left[1 + \cos\left(\frac{\phi}{f}\right) \right],\tag{22}$$

where, both Λ and f have dimension of mass. The prognostications of the natural potential on the CMB scale are not consistent with the latest data of Planck 2018 in the standard model of inflation [79, 80]. Accordingly, we strive to rectify its shortcomings on the CMB scale using the non-canonical parameters $\{\alpha, M_0\}$ of the GPLNC framework. The Λ and M_0 parameter are associated together through the SR relation of the scalar power spectrum (13).

Hence, fixing $\Lambda = 0.01 M_P$ to guarantee the correct energy scale of inflation, the parameter M_0 is attained from the CMB normalization confinement $\mathcal{P}_{\mathcal{R}}(k_*) \sim 2.1 \times 10^{-9}$ at pivot scale $(k_* = 0.05 \text{ Mpc}^{-1})$ [79]. The α parameter is responsible to cure the prognostications of the natural potential for r and n_s in the GPLNC setup. Table I is allotted to common fixed parameters for all cases of the model, while Table II contains the regulated parameter sets for each case. The computed values for n_s , r and related parameters to PBHs are listed in Table III.

TABLE I: Common fixed parameters for all cases of the model.

#	α	b/M_P	f/M_P	Λ/M_P
All cases	20	1.2×10^{-2}	2	0.01

TABLE II: Regulated parameters for all cases of the model.

#	ω	ϕ_c/M_P	M_0/M_P
Case A	14.895	5.8090	2.33×10^{-4}
Case B	15.220	5.7400	2.33×10^{-4}
Case C	15.440	5.6923	2.32×10^{-4}
Case D	13.100	5.7090	2.32×10^{-4}

TABLE III: Computed quantities corresponding to the cases of Tables I-II for n_s , r, $\mathcal{P}_{\mathcal{R}}^{\text{peak}}$, k_{peak} , $f_{\text{PBH}}^{\text{peak}}$ and $M_{\text{PBH}}^{\text{peak}}$. The values of n_s and r are evaluated at horizon intersecting e-folds number $N_* = 0$ by the pivot scale.

#	n_s	r	$\mathcal{P}_{\mathcal{R}}^{\mathrm{peak}}$	$k_{\rm peak}/{\rm Mpc}^{-1}$	$f_{ m PBH}^{ m peak}$	$M_{ m PBH}^{ m peak}/M_{\odot}$
Case A	0.9686	0.02	0.036	3.06×10^{12}	0.9963	2.52×10^{-13}
Case B	0.9686	0.02	0.043	3.59×10^8	0.0182	1.83×10^{-5}
Case C	0.9684	0.02	0.053	3.63×10^5	0.0016	17.88
Case D	0.9684	0.02	0.013	6.90×10^{6}	~ 0	0.0496

A. Background evolutions

So as to compute the results of Table III, we need to know the dynamics of background. Therefore, with numerical method, the equation of field evolution (9) thereto the 2nd Friedmann equation (6) are solved at once. Thence, developments of the scalar field ϕ , Hubble parameter H, field derivative $\phi_{,N}$, the 1st and 2nd slow-roll parameters (ε_1 and ε_2) versus e-folds number N for all cases of the model are computed and represented in Fig. 1.

It is inferable from Fig. 1 that (i) the inflationary era persists for ΔN e-folds number $(\Delta N = N_{\rm end} - N_*)$, between the horizon crossing moment by the pivot scale $(N_* = 0)$ and the end of inflation $(N_{\rm end})$. (ii) The end of inflation occurs through $\varepsilon_1 = 1$ for each case (Fig. 1(d)). (iii) The FR stage during a steep cliff in the field evolution pass in $\phi = \phi_c$ position is generated for each case of the model (Fig. 1(a)). (iv) In the FR stage, the speed of the inflaton increases (Fig. 1(c)). (v) The ε_1 parameter experiences a transient peak during the FR stage (see Fig. 1(d)). (vi) At the same time, the ε_2 parameter in the FR stage increases to large positive values and crosses $\varepsilon_2 = 1$, momentarily (see Fig. 1(e)). Hence the SR condition in FR stage is broken by ε_2 . (vii) Although the SR conditions $\{\varepsilon_1, \varepsilon_2\} \ll 1$ are broken in the FR stage, they are established around the CMB scale $N_* = 0$ (Figs. 1(d) and 1(e)).

Thus, computing the n_s and r via Eqs. (15) and (19), governed by the SR approximation, is permitted. According to the presented results in Table III, the values of n_s for all cases of the model lie inside the 68% CL of permitted data by Planck 2018 (TT, TE, EE+lowE+lensing+BK18+BAO) [79]. Moreover, r = 0.02 for each case of the model is consistent with the imposed upper bound on r by Planck and BICEP/Keck 2018 data (r < 0.036 at 95% CL) [80]. As a consequence, the GPLNC framework have succeeded to amend the observational predictions of the natural potential.

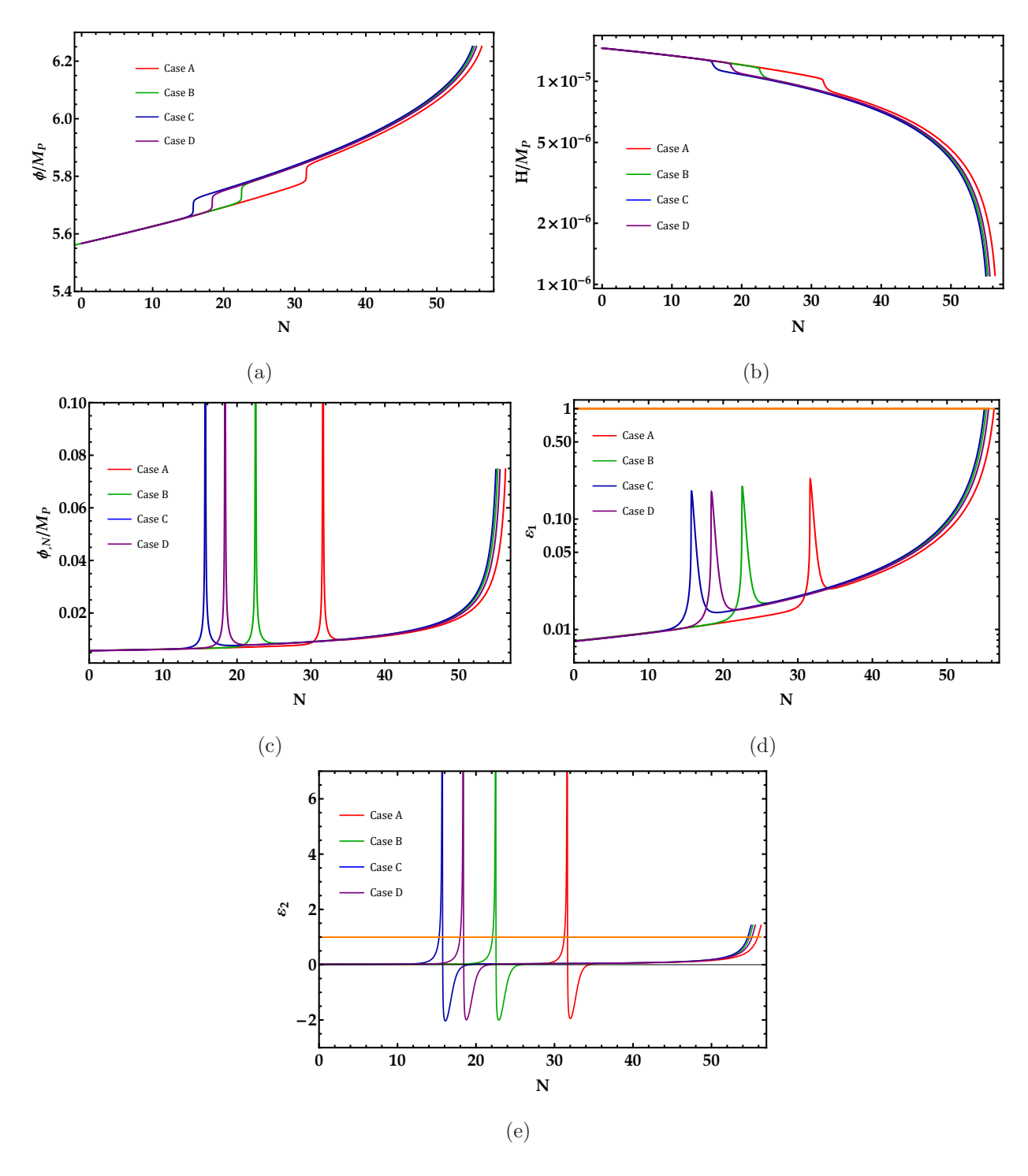


FIG. 1: Variations of (a) the scalar field, (b) the Hubble parameter, (c) the field derivative, (d) the first SR parameter and (e) the second SR parameter against the *e*-folds number N for cases A (red curves), B (green curves), C (blue curves) and D (purple curves).

In the following, we are interested in checking the swampland criteria for the model. The swampland criteria encompass two conjectures to wit distance conjecture and de-Sitter conjecture [81–83], which arise out of string theory. The distance conjecture imposes an upper limit on the field variation like $\Delta \phi/M_P < c_1$, while the de Sitter conjecture imposes a lower limit on the potential gradient like $M_P|V_{,\phi}/V| > c_2$. In these conjectures c_1 and c_2 are constants of order one. For the first conjecture, the field variation $\Delta \phi = \phi(N) - \phi(N_{\rm end})$ is evaluated and displayed in Fig. 2(a) for each case of the model. Apropos to the second conjecture, Fig. 2(b) illustrates the gradient of the inflationary potential $|V_{,\phi}/V|$ for cases of the model. The graphs of Fig. 2 indicate the validity of our model in light of the swampland criteria.

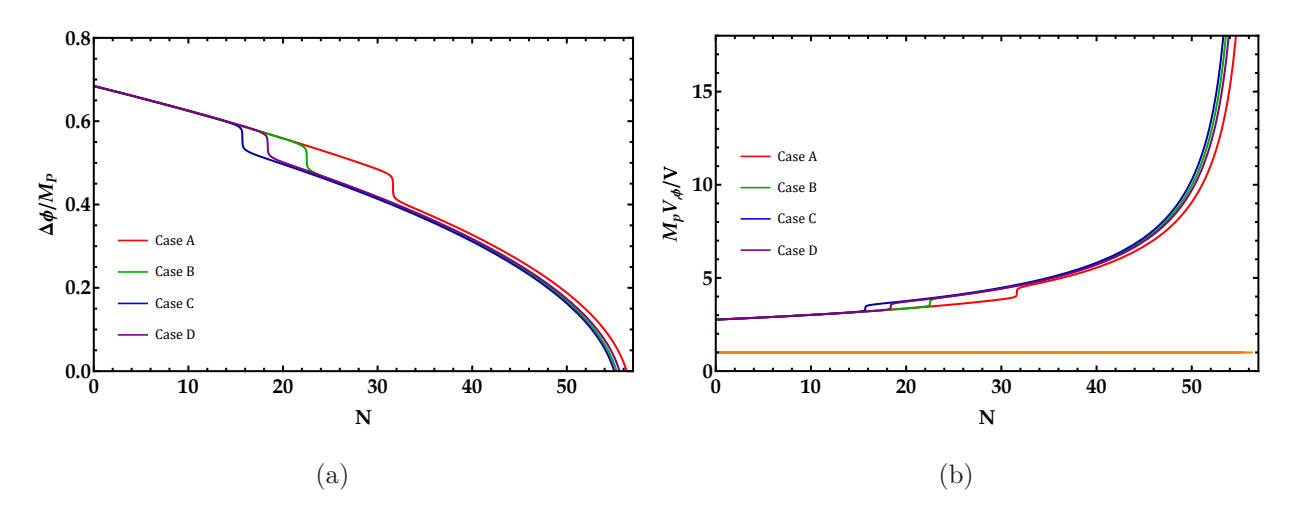


FIG. 2: Establishment of the swampland criteria for cases of the model encompass (a) the distance conjecture $\Delta \phi/M_P < c_1$ and (b) the de-Sitter conjecture $M_P|V_{,\phi}/V| > c_2$.

B. Evolutions of the scalar and tensor perturbations

In what follows, after analyzing the background evolution, we need to know the evolutions of the scalar and tensor power spectra. At first, we solve the MS equation (10) in numerical way to find the precise value of the curvature power spectrum from Eq. (12). Thence, we plot the outcomes in Fig. 3(a) with regard to wavenumber k for all cases of Table II in addition to the observational restrictions. Also the numerical values of the peaks of the scalar power spectra (at $\phi = \phi_c$) and their related wavenumbers are listed in Table III for all cases. Fig. 3(a) indicates that (i) the scalar power spectra adjacent to CMB scale $k_* \sim 0.05 \text{ Mpc}^{-1}$ for all cases satisfy the Planck confinement $\mathcal{P}_{\mathcal{R}}(k_*) \simeq 2.1 \times 10^{-9}$ [79]. (ii) The scalar power spectra respecting all cases experience large peaks with heights of order 10^{-2} adjacent to cliff positions ($\phi = \phi_c$) in the FR stages that are necessary to born PBHs

seeds.

So as to compute the tensor power spectra for cases of our model, we solve the tensor MS equation (16) in numerical way. Thence, the precise values of the tensor power spectrum are evaluated by Eq. (17). The numerical outcomes for \mathcal{P}_t are schemed with regard to wavenumber in Fig. 3(b). This figure indicates that (i) on the CMB scale $k_* \sim 0.05 \text{ Mpc}^{-1}$, the tensor-to-scalar ratio $r = \mathcal{P}_t(k_*)/\mathcal{P}_{\mathcal{R}}(k_*)$ results in consistent values with Table III computed by Eq. (19). (ii) The cliff-like region in the plot of the tensor power spectrum for each case originates from the cliff-like region in the Hubble parameter during the FR stage (see Fig. 1(b)).

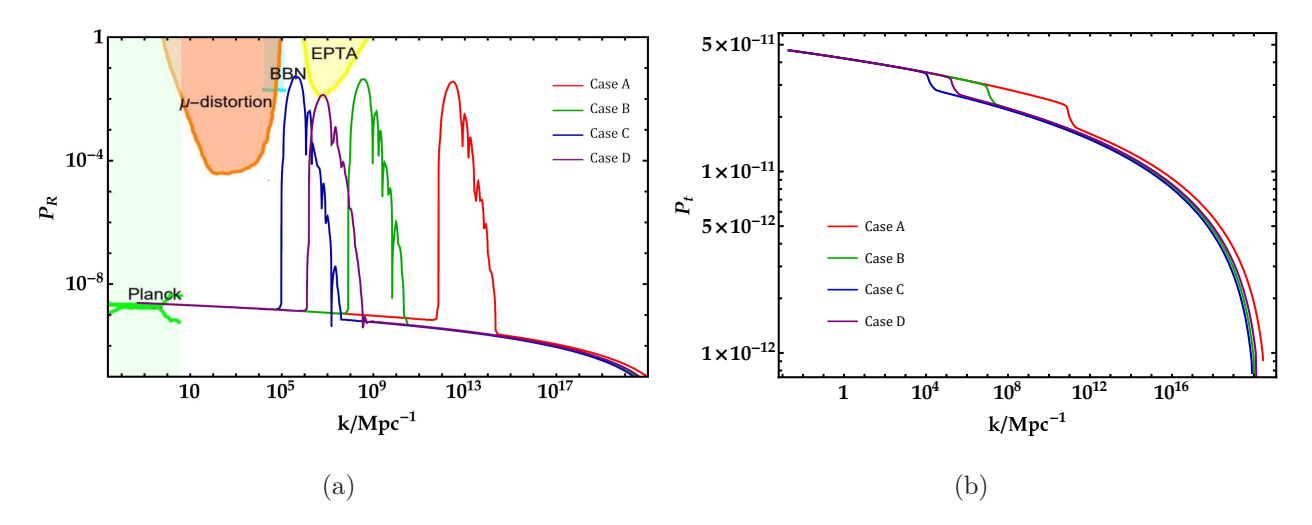


FIG. 3: (a) The curvature and (b) the tensor power spectra with regard to the comoving wavenumber k for Cases A (red curves), B (green curves), C (blue curves) and D (purple curves). The colory zones are prohibited through the CMB observations [79] (light-green), PTA observations [84] (yellow), the impact on the ration of neutron-to-proton in the course of Big Bang Nucleosynthesis (BBN) [85–87] (cyn), and the μ -distortion of CMB [88, 89] (orange).

IV. REHEATING CONSIDERATION

In this section, we are interested in analyzing the reheating era in order to know when the super-horizon perturbed scales revet to the horizon after inflation. Among the perturbed scale those ones pertinent to peaks of the curvature power spectrum (see Table III and blue circles in left panels of Fig. 4) are important due to their key role in producing PBHs seeds. A lengthy reheating era with low temperature after inflation may results in reverting the

peak scales to the horizon in the reheating stage rather than the RD era. Hence, analyzing the duration of reheating era $N_{\rm reh}$ and its temperature $T_{\rm reh}$ is essential. The duration of the reheating stage $N_{\rm reh}$ is specified by the e-folds number between the end of inflation and end of reheating and is related to the duration of the inflationary era $\Delta N = N_{\rm end} - N_*$ as follows [7, 11, 25, 26, 77]

$$N_{\rm reh} = \frac{4}{1 - 3\omega_{\rm reh}} \left[61.6 - \ln\left(\frac{\rho_{\rm end}}{H_*}\right) - \Delta N \right], \tag{23}$$

where, $\omega_{\rm reh}$ is the equation of state parameter of the reheating stage and it is taken as $\omega_{\rm reh} = 0$ in this model. The energy density in the end of inflation is computed through $\rho_{\rm end} = 3M_P^2 H_{\rm end}^2$ and H_* is the Hubble parameter at the horizon leaving e-fold number $N_* = 0$ by the pivot scale $k_* \sim 0.05 \; {\rm Mpc^{-1}}$. Pursuant to [7, 11, 25, 26, 77], using $N_{\rm reh}$ the reheating temperature is calculated as

$$T_{\rm reh} = \left(\frac{30}{\pi^2 g_*} \rho_{\rm end}\right)^{1/4} \exp\left[-\frac{3}{4} (1 + \omega_{\rm reh}) N_{\rm reh}\right],$$
 (24)

in which $g_* = 106.75$ denotes the effective number of relativistic degree of freedom in the energy density in reheating stage. Table IV contains the computed values for $N_{\rm reh}$ and $T_{\rm reh}$ as to each case of the model. Furthermore, this Table embodies duration of the inflationary era ΔN , the e-fold number $N_k^{\rm peak}$ and wavenumber $k_{\rm peak}$ as to the peak position of the curvature power spectrum (at $\phi = \phi_c$ corresponding to the blue circles in left panels of Fig. 4) and $k_{\rm reh}$ as well. The $k_{\rm reh}$ indicates the wavenumber of the reverting scale to the horizon at end of reheating era and is computed as [25]

$$k_{\rm reh} = e^{-N_{\rm reh}/2} k_{\rm end}, \tag{25}$$

wherein, k_{end} is the wavenumber of the scale that exits from (reverts to) the horizon at the end of inflation.

In what follows, we attempt to show that in our model the scales pertinent to PBHs seeds (blue circles in left panels of Fig. 4) revert to the horizon in RD era after reheating stage. To this end, the scale $k_{\rm reh}^{-1}$ is calculated for each case of the model and compared to the peak scale $k_{\rm peak}^{-1}$ of that case. It is known that, the larger scales with larger k^{-1} leave the horizon earlier and thereafter revert to the horizon later than smaller scales with smaller k^{-1} . As regards $k_{\rm reh}^{-1}$ corresponds to the scale which reverts to the horizon at the end of reheating, thus each scale larger than $k_{\rm reh}^{-1}$ revert to the horizon after the reheating era in RD or MD

era. Therefore, drawing a comparison between the listed values of k_{reh} and k_{peak} in Table IV illustrates that the peak scale for each case is larger than k_{reh}^{-1} . As a result, the peak scales for all cases of our model revert to horizon in RD era after reheating to produce PBHs.

The above outcomes are exhibited in Fig. 4 as well. In this figure, the curvature power spectra versus k in the left panels and comoving Hubble radius versus N in right panels are schemed for all cases of the model. Altogether in Fig. 4, (i) the shadowy portions in all panels indicate the scales which re-enter the horizon during the reheating stages. (ii) The red, blue and green circles on the curvature power spectra in the left panels depict, respectively, the pivot scale $k_* \sim 0.05 \text{ Mpc}^{-1}$, the peak scale k_{peak} and the reverting scale to the horizon in the end of reheating era k_{reh} . (iii) The red, blue and green circles in right panels indicate exit from (revert to) the horizon as to the scales k_*^{-1} , k_{peak}^{-1} and k_{reh}^{-1} , respectively. Consequently, the PBHs scales in our model revert to the horizon in RD era to produce ultra-dense portions to collapse and born PBHs.

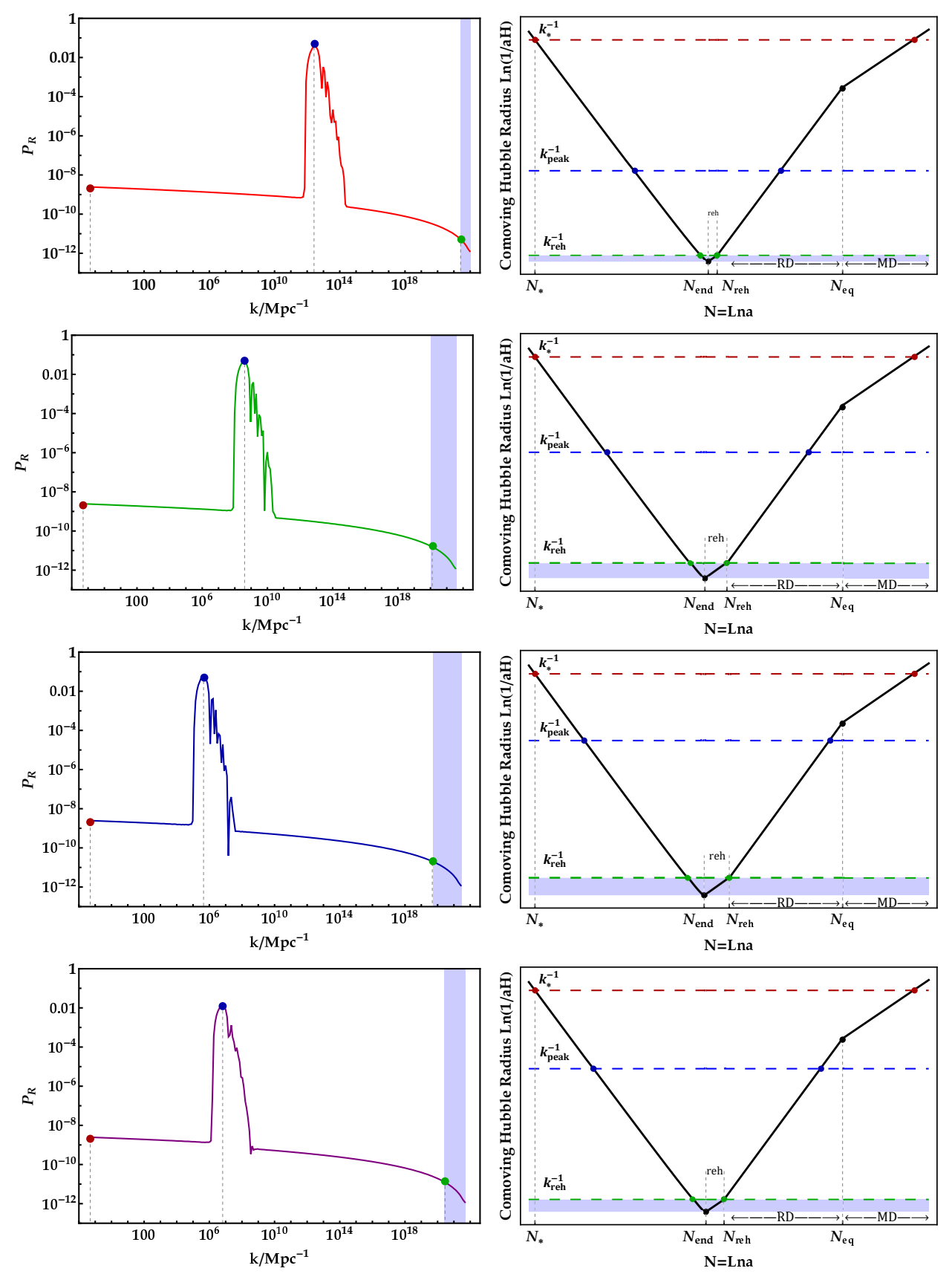


FIG. 4: (Left) The curvature power spectra with regard to wavenumber k for cases A (red curve), B (green curve), C (blue curve) and D (purple curve). Here, the red, blue and green circles depict k_* , k_{peak} and k_{reh} . (Right) The comoving Hubble radius against N, in which the red, blue and green circles depict the horizon leaving (reverting) for the scales k_*^{-1} , k_{peak}^{-1} and k_{reh}^{-1} , respectively. The shadowy portions correspond to the reverting scales to the horizon during the reheating stage.

				10 1		_
#	ΔN	$N_{ m reh}$	$N_k^{ m peak}$	$k_{\rm peak}/{\rm Mpc^{-1}}$	$k_{ m reh}/{ m Mpc^{-1}}$	$T_{ m reh}/{ m GeV}$
Case A	56.32	2.90	32.2	3.06×10^{12}	2.56×10^{21}	1.56×10^{14}
Case B	55.26	7.13	23.0	3.59×10^{8}	1.07×10^{20}	6.56×10^{12}
Case C	55.01	8.15	16.0	3.63×10^5	4.98×10^{19}	3.04×10^{12}
Case D	55.57	5.90	19.0	6.90×10^{6}	2.69×10^{20}	1.65×10^{13}

TABLE IV: The quantities of ΔN , $N_{\rm reh}$, $N_k^{\rm peak}$, $k_{\rm peak}$, $k_{\rm reh}$ and $T_{\rm reh}$ as to all cases of the model.

PBHS ABUNDANCES

In the erstwhile section, the curvature power spectra for cases of the GPLNC natural inflationary model are computed through the FR mechanism. Here, using the computed values for $\mathcal{P}_{\mathcal{R}}$, the PBHs abundance f_{PBH} and mass M_{PBH} are evaluated. The PBHs abundance $f_{\rm PBH} \equiv \Omega_{\rm PBH}/\Omega_{\rm DM}$ specifies that, what percentage of the current DM budget of the cosmos is allotted to PBHs. The current density parameter of DM is defined by Planck 2018 data as $\Omega_{\rm DM}h^2 \simeq 0.12$ [79]. The fractional PBHs abundance is given by

$$f_{\rm PBH}(M) \equiv \frac{\Omega_{\rm PBH}}{\Omega_{\rm DM}} = \frac{\beta(M)}{1.84 \times 10^{-8}} \left(\frac{\gamma}{0.2}\right)^{3/2} \left(\frac{g_*}{10.75}\right)^{-1/4} \left(\frac{0.12}{\Omega_{\rm DM}h^2}\right) \left(\frac{M}{M_{\odot}}\right)^{-1/2}, \quad (26)$$

where, $\gamma = (1/\sqrt{3})^3$ signifies the collapse efficacy parameter [90] and $g_* = 106.75$ is the effective number of relativistic degrees of freedom. Moreover, considering the gaussian distribution for the primordial perturbations, $\beta(M)$ the production rate of PBHs is computed through the Press-Schechter formulation as [91, 92]

$$\beta(M) = \int_{\delta_c}^{\infty} \frac{\mathrm{d}\delta}{\sqrt{2\pi\sigma^2(M)}} e^{-\frac{\delta^2}{2\sigma^2(M)}} = \frac{1}{2} \operatorname{erfc}\left(\frac{\delta_c}{\sqrt{2\sigma^2(M)}}\right),\tag{27}$$

where "erfc" is the error function complementary and $\delta_c = 0.4$ is the density threshold [93, 94]. Additionally, $\sigma^2(M)$ is the smoothed density contrast on scale k and it is related to the curvature power spectrum $\mathcal{P}_{\mathcal{R}}$ and Gaussian window function $W(x) = \exp(-x^2/2)$ as follows

$$\sigma_k^2 = \left(\frac{16}{81}\right) \int_0^\infty \frac{\mathrm{d}q}{q} W^2(q/k) (q/k)^4 \mathcal{P}_{\mathcal{R}}(q). \tag{28}$$

At last M in Eq. (26) expresses the PBHs mass and is associated to the horizon mass as

$$M(k) \equiv \gamma M_{\text{horizon}} \simeq M_{\odot} \left(\frac{\gamma}{0.2}\right) \left(\frac{10.75}{g_*}\right)^{\frac{1}{6}} \left(\frac{k}{1.9 \times 10^6 \text{Mpc}^{-1}}\right)^{-2}.$$
 (29)

Thereafter, we are able to calculate the abundances f_{PBH} and masses M_{PBH} of PBHs as to cases of Table II, using the obtained $\mathcal{P}_{\mathcal{R}}$ and Eqs. (26)-(29). The numerical results for $f_{\text{PBH}}^{\text{peak}}$ and $M_{\text{PBH}}^{\text{peak}}$ (corresponding to peak spot $\phi = \phi_c$) are sorted into Table III. Into the bargain, in Fig. 5 the evaluated results for f_{PBH} with regard to M_{PBH} in addition to observational restricted portions are plotted for all cases. This figure illustrates that, (i) the corresponding PBH to case A (red curve) with $f_{\text{PBH}}^{\text{peak}} \sim 1$ could comprise all DM budget of the universe. (ii) The mass spectrum of PBH as to case B (green curve) has lied in the allowed data of OGLE [47, 48], so it could be a considerable source for ultrashort-timescale microlensing events. (iii) The current GWs spectrum propagated from PBH as to case C (blue curve) could be tracked down by LIGO and Virgo interferometers, hence this case of PBHs could be a considerable origin for LIGO-Virgo events. It is notable that, the abundance of PBH as to case D is of order 10^{-27} and it has a trivial contribution in DM budget.

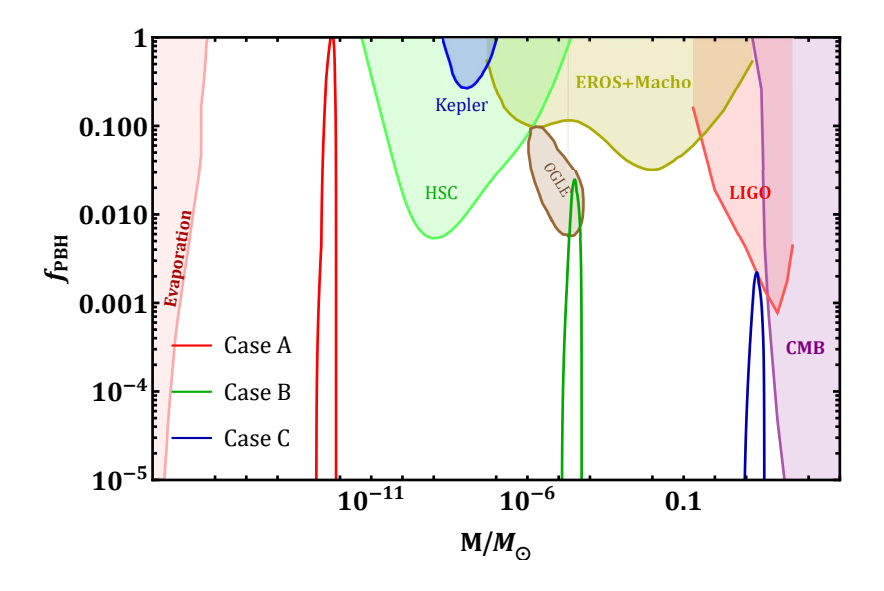


FIG. 5: The PBHs mass spectra concerning cases A (red curve), B (green curve) and C (blue curve). The observational restricted portions are demonstrated by colory domains. The disallowed portions are prohibited by observations of CMB [95] (purple portion), LIGO-VIRGO event [96–99] (red portion), microlensing events through MACHO [100] and EROS [101] (khaki portion), Kepler [102]) (blue portion), Icarus [103], OGLE [47, 48] and Subaru-HSC [104] (green portion), and PBHs evaporation [23, 105–108] (pink portion). The sol permissible portion (brown portion) in the plot is defined by the ultrashort-timescale microlensing events in the OGLE data [47, 48].

VI. COEVAL GRAVITATIONAL WAVES WITH PBHS

Concurrent with generation of the seeds of PBHs in RD era, secondary GWs propagate in the universe. The density spectrum of these GWs could be traced via various observatories such as SKA [109], EPTA [110–113], LISA [114, 115], BBO [116, 117] and DECIGO [116, 118] at present. Thus, PBHs in different masses could be detected by way of propagated secondary GWs, indirectly. In this section, the density spectra of secondary GWs as to generated PBHs in natural GPLNC inflationary model are evaluated. the present-time GWs density parameter Ω_{GW_0} at η_0 , is associated with its match at time η as follows (η signifies the conformal time) [84]

$$\Omega_{\text{GW}_0} h^2 = 0.83 \left(\frac{g_*}{10.75} \right)^{-1/3} \Omega_{\text{r}_0} h^2 \Omega_{\text{GW}}(\eta, k), \tag{30}$$

therein, $g_* \simeq 106.75$ expresses the effective degrees of freedom in the energy density at η and $\Omega_{\rm r_0}h^2 \simeq 4.2 \times 10^{-5}$ is the present-time density parameter of radiation. Moreover, $\Omega_{\rm GW}(\eta, k)$ is calculated via [119, 120]

$$\Omega_{\rm GW}(k,\eta) = \frac{1}{6} \left(\frac{k}{aH}\right)^2 \int_0^\infty dv \int_{|1-v|}^{|1+v|} du \left(\frac{4v^2 - (1-u^2+v^2)^2}{4uv}\right)^2 \overline{I_{RD}^2(u,v,x)} \mathcal{P}_{\mathcal{R}}(ku) \mathcal{P}_{\mathcal{R}}(kv),$$
(31)

where, the time-mean of the source term is expressed by

$$\frac{I_{RD}^{2}(u,v,x\to\infty)}{I_{RD}^{2}(u,v,x\to\infty)} = \frac{1}{2x^{2}} \left[\left(\frac{3\pi \left(u^{2}+v^{2}-3\right)^{2} \Theta\left(u+v-\sqrt{3}\right)}{4u^{3}v^{3}} + \frac{T_{c}(u,v,1)}{9} \right)^{2} + \left(\frac{\tilde{T}_{s}(u,v,1)}{9} \right)^{2} \right].$$
(32)

In the above equation, Θ expresses the Heaviside step function where, $\Theta(x) = 0$ for x < 0 and $\Theta(x) = 1$ for $x \ge 0$. Furthermore, T_c and T_s are specified as follows

$$T_{c} = -\frac{27}{8u^{3}v^{3}x^{4}} \left\{ -48uvx^{2}\cos\left(\frac{ux}{\sqrt{3}}\right)\cos\left(\frac{vx}{\sqrt{3}}\right) \left(3\sin(x) + x\cos(x)\right) + 48\sqrt{3}x^{2}\cos(x) \left(v\sin\left(\frac{ux}{\sqrt{3}}\right)\cos\left(\frac{vx}{\sqrt{3}}\right) + u\cos\left(\frac{ux}{\sqrt{3}}\right)\sin\left(\frac{vx}{\sqrt{3}}\right)\right) + 8\sqrt{3}x\sin(x) \left[v\left(18 - x^{2}\left(u^{2} - v^{2} + 3\right)\right)\sin\left(\frac{ux}{\sqrt{3}}\right)\cos\left(\frac{vx}{\sqrt{3}}\right) + u\left(18 - x^{2}\left(-u^{2} + v^{2} + 3\right)\right)\cos\left(\frac{ux}{\sqrt{3}}\right)\sin\left(\frac{vx}{\sqrt{3}}\right)\right] + 24x\cos(x)\left(x^{2}\left(-u^{2} - v^{2} + 3\right) - 6\right)\sin\left(\frac{ux}{\sqrt{3}}\right)\sin\left(\frac{vx}{\sqrt{3}}\right) + 24\sin(x)\left(x^{2}\left(u^{2} + v^{2} + 3\right) - 18\right)\sin\left(\frac{ux}{\sqrt{3}}\right)\sin\left(\frac{vx}{\sqrt{3}}\right) + 24\sin(x)\left(x^{2}\left(u^{2} + v^{2} + 3\right) - 18\right)\sin\left(\frac{ux}{\sqrt{3}}\right) + 2\sin(x)\left(x^{2}\left(u^{2} + v^{2} + 3\right) + 3\cos(x)\left(x^{2}\left(u^{2} + v^{2} + 3\right)\right) + 3\cos(x)\left(x^{2}\left(u^{2} + v^{2}\right)\right) + 3\cos(x)\left(x^{2}\left(u^{2} + v^{2}\right)\right) + 3\cos(x)\left(x^{2}\left(u^{2} + v^{2}\right)\right) + 3\cos(x)\left(x^{2}\left($$

$$T_{s} = \frac{27}{8u^{3}v^{3}x^{4}} \left\{ 48uvx^{2} \cos\left(\frac{ux}{\sqrt{3}}\right) \cos\left(\frac{vx}{\sqrt{3}}\right) \left(x \sin(x) - 3\cos(x)\right) - 48\sqrt{3}x^{2} \sin(x) \left(v \sin\left(\frac{ux}{\sqrt{3}}\right) \cos\left(\frac{vx}{\sqrt{3}}\right) + u \cos\left(\frac{ux}{\sqrt{3}}\right) \sin\left(\frac{vx}{\sqrt{3}}\right)\right) + 8\sqrt{3}x \cos(x) \left[v \left(18 - x^{2} \left(u^{2} - v^{2} + 3\right)\right) \sin\left(\frac{ux}{\sqrt{3}}\right) \cos\left(\frac{vx}{\sqrt{3}}\right) + u \left(18 - x^{2} \left(-u^{2} + v^{2} + 3\right)\right) \cos\left(\frac{ux}{\sqrt{3}}\right) \sin\left(\frac{vx}{\sqrt{3}}\right)\right] + 24x \sin(x) \left(6 - x^{2} \left(-u^{2} - v^{2} + 3\right)\right) \sin\left(\frac{ux}{\sqrt{3}}\right) \sin\left(\frac{vx}{\sqrt{3}}\right) + 24\cos(x) \left(x^{2} \left(u^{2} + v^{2} + 3\right) - 18\right) \sin\left(\frac{ux}{\sqrt{3}}\right) \sin\left(\frac{vx}{\sqrt{3}}\right) - \frac{27\left(u^{2} + v^{2} - 3\right)}{u^{2}v^{2}} + \frac{\left(27\left(u^{2} + v^{2} - 3\right)^{2}\right)}{4u^{3}v^{3}} \left\{-\operatorname{Ci}\left[\left|1 - \frac{u + v}{\sqrt{3}}\right|x\right] + \ln\left|\frac{3 - \left(u + v\right)^{2}}{3 - \left(u - v\right)^{2}}\right| + \operatorname{Ci}\left[\left(\frac{u - v}{\sqrt{3}} + 1\right)x\right] - \operatorname{Ci}\left[\left(\frac{u + v}{\sqrt{3}} + 1\right)x\right] + \operatorname{Ci}\left[\left(1 - \frac{u - v}{\sqrt{3}}\right)x\right]\right\}, \tag{34}$$

where, the sine-integral Si(x) and cosine-integral Ci(x) functions are designated via

$$\operatorname{Si}(x) = \int_0^x \frac{\sin(y)}{y} dy, \qquad \operatorname{Ci}(x) = -\int_x^\infty \frac{\cos(y)}{y} dy. \tag{35}$$

Additionally, the function $\tilde{T}_s(u, v, 1)$ is specified as

$$\tilde{T}_s(u,v,1) = T_s(u,v,1) + \frac{27(u^2 + v^2 - 3)}{u^2 v^2} - \frac{27(u^2 + v^2 - 3)^2}{4u^3 v^3} \ln \left| \frac{3 - (u+v)^2}{3 - (u-v)^2} \right|.$$
(36)

In the end, the wavenumber can be changed to frequency from $f=1.546\times 10^{-15}\,(k/{\rm Mpc}^{-1})\,{\rm Hz}.$

In this stage, we are able to calculate the present-time density spectra of secondary GWs relevant to all cases of the model via the numerical values of $\mathcal{P}_{\mathcal{R}}$ and Eqs. (30)-(36). The numerical outcomes for Ω_{GW_0} with regard to frequency have been illustrated with diagram of Fig. 6 for cases A (red curve), B (green curve), C (blue curve), D(purple curve). In addition, in this figure the sensibility dominions of GWs observatories are shown by purple (SKA), brown (EPTA), orange (LISA), green (BBO) and red (DECIGO) areas. Moreover, the shadowy gray area in Fig. 6 represents the dominion of NANOGrav 15 year data. It is inferred from Fig. 6 that, (i) the Ω_{GW_0} spectrum related to case A can be detected in

light of the oncoming data of LISA, DICIEGO and BBO observatories. (ii) The spectra of $\Omega_{\rm GW_0}$ related to cases B, C and D could be ferreted out through the SKA detector. (iii) The peak of $\Omega_{\rm GW_0}$ for case D lies inside the NANOGrav 15 year and PPTA data, hence this case can be contemplated as a promising origin for the low-frequency GWs signals found by NANOGrav, EPTA, PPTA and CPTA [49–58]. (iv) The $\Omega_{\rm GW_0}$ spectra show power-like functioning with regard to frequency f in various frequency ranges (see the black dashed line fitted on the $\Omega_{\rm GW_0}$ spectra of cases A and D).

Into the bargain, the frequencies of the peaks of $\Omega_{\rm GW_0}$ spectra (f_c) as well as the peak values for $\Omega_{\rm GW_0}$ as to all cases of the model are arranged in Table V. It is proven that, the $\Omega_{\rm GW_0}$ spectrum exhibits the power-like functioning versus the frequency as $\Omega_{\rm GW_0}(f) \sim f^n$ [15, 121, 122]. The evaluated exponents n in frequencies scopes $f \ll f_c$, $f < f_c$ and $f > f_c$ for all cases of the model have been registered in Table V. It is deduced from the sorted data in this table that, the evaluated exponents n in the infrared frequency scope $f \ll f_c$ for all cases of the model satisfy the logarithmic relation $n = 3 - 2/\ln(f_c/f)$ analyzed in [123–125]. Furthermore, the exponent n in the NANOGrav dominion for frequency scope $f < f_c$ is related to spectral index γ as $n = 5 - \gamma$. The imposed constraint on γ by the NANOGrav collaboration is $\gamma = 3.2 \pm 0.6$ [49–53]. Ergo, the exponent n = 1.58 for case D of our model results in $\gamma = 3.42$ which satisfies the NANOGrav constraint (see Table V and Fig. 6).

TABLE V: The peak values of frequencies and $\Omega_{\rm GW_0}h^2$ spectra, in addition to the exponent n in frequency ranges $f \ll f_c$, $f < f_c$ and $f > f_c$ regarding cases A, B, C and D.

#	$f_c/{ m Hz}$	$\Omega_{\mathrm{GW}_{0}}h^{2}\left(f_{c}\right)$	$n_{f \ll f_c}$	$n_{f < f_c}$	$n_{f>f_c}$
Case A	4.74×10^{-3}	9.37×10^{-9}	3.05	1.67	-4.74
Case B	6.68×10^{-7}	1.35×10^{-8}	3.09	1.57	-1.65
Case C	8.12×10^{-10}	2.18×10^{-8}	3.06	1.67	-1.81
Case D	1.07×10^{-8}	1.26×10^{-9}	3.07	1.58	-1.67

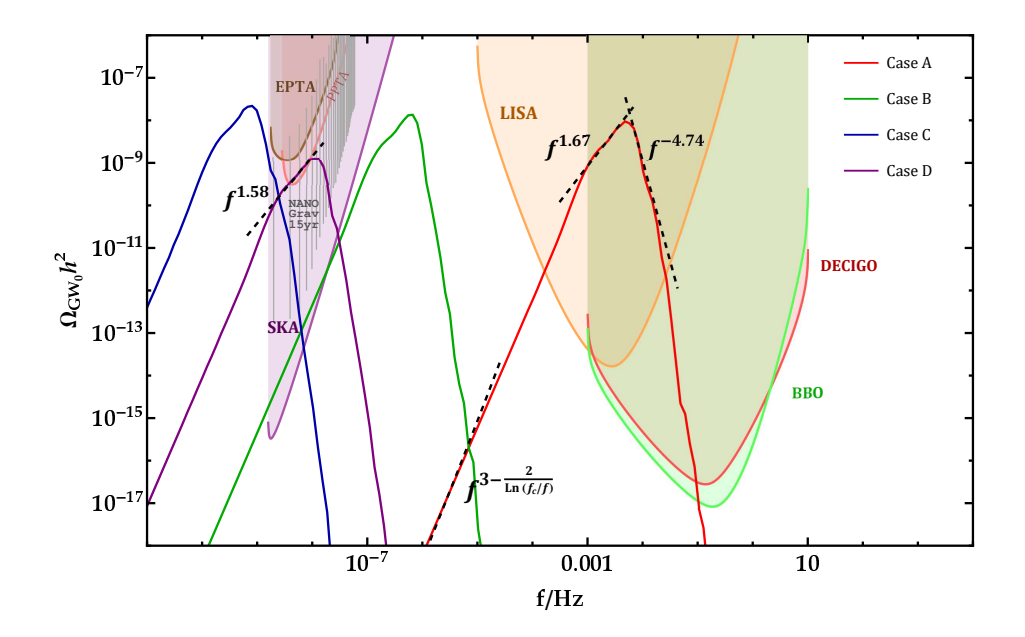


FIG. 6: The present-time density spectra of secondary gravitational waves $\Omega_{\rm GW_0}h^2$ with regard to frequency for cases A (red curve), B (green curve), C (blue curve) and D (Purple curve) as well as the observational dominions of EPTA (brown domain), SKA (purple domain), NANOGrav 15 year data (gray shadowy area) LISA (orange domain), DECIGO (red domain) and BBO (green domain). The power-like functioning of $\Omega_{\rm GW_0}h^2$ spectra have been represented by dashed black lines in various frequencies ranges according to Table V for cases A and D.

VII. CONCLUSIONS

In this paper, production of PBHs and GWs in GPLNC natural inflationary model through FR mechanism was probed. In this model, employing the non-canonical mass scale parameter $M(\phi)$ of the power-law Lagrangian (2) as a twofold function of the scalar field (20)-(21), a cliff-like region was produced in the field evolution path. When the scalar field fall off the cliff, its kinetic energy increases and a transient FR stage is produced which lasts for about one e-fold or less (see Figs. 1(a) and 1(c)). While the non-adiabatic transition in the field evolution from the SR to FR stage takes place, the particle production results in enhancing the scalar perturbations in the FR stage. Thereafter, horizon reverting of the enhanced scale during the RD era gives rise to produce PBHs seeds. The parameter M_0 in $M(\phi)$ and non-canonical α parameter are responsible for reviving the natural potential on CMB scale in this model. On the other side, the other parameters of $M(\phi)$ like $\{\omega, \phi_c, d\}$

are responsible to produce the suitable cliff-like region in $(\phi = \phi_c)$ for accelerating the scalar field in the FR stage to produce PBHs. These three parameters do not affect the CMB scale. During the FR stage, the ε_1 encounters a peaked enhancement, although it remains smaller than one and loyal to the SR condition all over the inflationary era. On the contrary, the ε_2 breaks the SR condition and increases to larger values than one during the FR stage (see Figs. 1(d) and 1(e)). The main consequences of the chosen model are as follows

- The observational predictions of natural potential in this framework satisfy constraints of Planck and BICEP/Keck 2018 (TT,TE,EE+lowE+lensing+BK18+BAO) at 68% CL for the scalar spectral index n_s and 95% for the tensor-to-scalar ratio r [79, 80] (note to Table III).
- Two theoretical conjectures of the swampland criteria are established for this model (see plots of Fig. 2).
- Solving the MS equations (10) and (16) results, respectively, in obtaining the curvature and tensor power spectra for each case of the model. The curvature spectra $\mathcal{P}_{\mathcal{R}}$ for all cases of the model on the CMB scale $k_* \sim 0.05 \;\mathrm{Mpc^{-1}}$ are of order 10^{-9} in consistency with Planck 2018 observations [79], whereas on smaller scale near $\phi = \phi_c$ (in the FR stage) have peaks of order 10^{-2} which are required to produce PBHs (see Fig. 3). Also the results of tensor-to-scalar ratio $r = \mathcal{P}_t(k_*)/\mathcal{P}_{\mathcal{R}}(k_*)$ for aforementioned model are well compatible with Planck and BICEP/Keck 2018 data.
- Through the reheating considerations, it was proven that the peak scales related to PBHs formation revert to the horizon in RD era to produce PBHs scales (see Fig. 4).
- Three cases of PBHs proper for explaining the DM budget, microlensing events in OGLE data and LIGO/Virgo events are predicted by this model (see Table III and Fig. 5).
- The present-time density spectra Ω_{GW_0} of coeval secondary GWs with PBHs generation could intersect the sensitivity curves of various GWs observatories in various frequency ranges (see Fig. 6).
- The power-like functioning as $\Omega_{GW_0}(f) \sim f^n$ in different frequency zones for all cases of the model were indicated (see Table V and Fig. 6).

- In the infrared regime $f \ll f_c$, the exponent n satisfies the logarithmic relation $n = 3 2/\ln(f_c/f)$ (see Table V and Fig. 6).
- The present-time density spectrum of case D is located in the NANOGrav 15 year and PPTA data domain (see Fig. 6), and it can be a suitable source for low-frequency GWs detected by NANOGrav, EPTA and PPTA teamwork.
- Regarding the relation $n = 5 \gamma$ in the frequency scope $f < f_c$ of the NANOGrav domain, the evaluated exponent n = 1.58 for case D results in $\gamma = 3.42$ which satisfies the constraint of NANOGrav collaboration for spectral index as $\gamma = 3.2 \pm 0.6$ [49–53].
- [1] A. Y. Kamenshchik, A. Tronconi, T. Vardanyan, and G. Venturi, Phys. Lett. B **791**, 201 (2019).
- [2] T. Papanikolaou, A. Lymperis, S. Lola, and E. N. Saridakis, J. Cosmol. Astropart. Phys. 03, 003 (2023).
- [3] S. Heydari and K. Karami, Eur. Phys. J. C 84, 127 (2024).
- [4] S. Heydari and K. Karami, J. Cosmol. Astropart. Phys. **02** 047 (2024).
- [5] M. Solbi and K. Karami, Eur. Phys. J. C 81, 884 (2021).
- [6] M. Solbi and K. Karami, J. Cosmol. Astropart. Phys. 08, 056 (2021).
- [7] M. Solbi and K. Karami, arXiv:2403.00021.
- [8] Z. Teimoori, K. Rezazadeh, M. A. Rasheed, and K. Karami, J. Cosmol. Astropart. Phys. 10, 018 (2021).
- [9] C. Fu, P. Wu, and H. Yu, Phys. Rev. D **100**, 063532 (2019).
- [10] Z. Teimoori, K. Rezazadeh, and K. Karami, Astrophys. J. 915, 118 (2021).
- [11] S. Heydari and K. Karami, Eur. Phys. J. C 82, 83 (2022).
- [12] S. Heydari and K. Karami, J. Cosmol. Astropart. Phys. 03, 033 (2022).
- [13] I. Dalianis, S. Karydas, and E. Papantonopoulos, J. Cosmol. Astropart. Phys. **06**, 040 (2020).
- [14] A. Ashrafzadeh, K. Karami, Astrophys. J. **965**, 11 (2024).
- [15] C. Fu, P. Wu, and H. Yu, Phys. Rev. D **101**, 023529 (2020).
- [16] S. Pi, Y. Zhang, M. Sasaki and Q. G. Huang, J. Cosmol. Astropart. Phys. 05, 042 (2018).
- [17] S. Kawai and J. Kim, Phys. Rev. D **104**, 083545 (2021).

- [18] R. Kawaguchi and S. Tsujikawa, Phys. Rev. D **107**, 063508 (2023).
- [19] S. Clesse and J. Garcia-Bellido, Phys. Rev. D **92**, 023524 (2015).
- [20] M. Braglia, D. K. Hazra, F. Finelli, G. F. Smoot, L. Sriramkumar, and A. A. Starobinsky, J. Cosmol. Astropart. Phys. 08 001 (2020).
- [21] S. Kawai and J. Kim, Phys. Rev. D 107, 043523 (2023).
- [22] M. Kawasaki, A. Kusenko, Y. Tada, and T. T. Yanagida, Phys. Rev. D 94, 083523 (2016).
- [23] R. Laha, Phys. Rev .Lett. **123**, 251101 (2019).
- [24] S. S. Mishra and V. Sahni, J. Cosmol. Astropart. Phys. **04**, 007 (2020).
- [25] I. Dalianis, A. Kehagias, and G. Tringas, J. Cosmol. Astropart. Phys. 01, 037 (2019).
- [26] R. Mahbub, Phys. Rev. D **101**, 023533 (2020).
- [27] H. Motohashi and W. Hu, Phys. Rev. D **96**, 063503 (2017).
- [28] J. Garcia-Bellido, M. Peloso, and C. Unal, J. Cosmol. Astropart. Phys. 09, 013 (2017)
- [29] K. Rezazadeh, Z. Teimoori, and K. Karami, Eur. Phys. J. C 82, 758 (2022).
- [30] X. Wang, Y. l. Zhang, R. Kimura, and M. Yamaguchi, Sci. China Phys. Mech. Astron. 66, 260462 (2023).
- [31] M. Drees and Y. Xu, Eur. Phys. J. C **81**, 182 (2021).
- [32] G. Domènech and S. Pi, M. Sasaki, Int. J. Mod. Phys. D 29, 2050028 (2020).
- [33] G. Domènech and S. Pi, M. Sasaki, J. Cosmol. Astropart. Phys. 08, 017 (2020).
- [34] G. Domènech, Universe 7, 398 (2021).
- [35] C. Yuan, Q. G. Huang, iScience **24**, 102860 (2021).
- [36] M. Yu. Khlopov, Res. Astron. Astrophys. 10, 495 (2010).
- [37] K. M. Belotsky et al., Mod. Phys. Lett. A 29, 1440005 (2014).
- [38] K. M. Belotsky et al., Eur. Phys. J. C 79, 246 (2019).
- [39] S. Choudhury, S. Panda, and M. Sami, Phys. Lett. B 845, 138123 (2023).
- [40] S. Choudhury, S. Panda, and M. Sami, J. Cosmol. Astropart. Phys. 08, 078 (2023).
- [41] W. Ahmed, M. Junaid, and U. Zubair, Nucl. Phys. B 984, 115968 (2022).
- [42] B. P. Abbott et al. (LIGO Scientific Collaboration and Virgo Collaboration), Phys. Rev. Lett. 116, 061102 (2016).
- [43] B. P. Abbott *et al.* (LIGO Scientific Collaboration and Virgo Collaboration), Phys. Rev. Lett. **116**, 241103 (2016).
- [44] B. P. Abbott et al. (LIGO Scientific Collaboration and Virgo Collaboration), Phys. Rev.

- Lett. 116, 221101 (2017).
- [45] B. P. Abbott et al. (LIGO Scientific Collaboration and Virgo Collaboration), Astrophys. J. 851, L35 (2017).
- [46] B. P. Abbott et al. (LIGO Scientific Collaboration and Virgo Collaboration), Phys. Rev. Lett. 119, 141101 (2017).
- [47] H. Niikura, M. Takada, S. Yokoyama, T. Sumi, and S. Masaki, Phys. Rev. D 99, 083503 (2019).
- [48] P. Mróz, U. Andrzej, and S. Jan et al., Nature **548**, 183–186 (2017).
- [49] Z. Arzoumanian et al. (NANOGrav Collaboration), Astrophys. J. Lett. 905, L34 (2020).
- [50] G. Agazie et al. (NANOGrav Collaboration), Astrophys. J. Lett. 951, L8 (2023).
- [51] G. Agazie et al. (NANOGrav Collaboration), Astrophys. J. Lett. 951, L9 (2023).
- [52] G. Agazie et al. (NANOGrav Collaboration), Astrophys. J. Lett. 951, L10 (2023).
- [53] G. Agazie et al. (NANOGrav Collaboration), Astrophys. J. Lett. 951, L11 (2023).
- [54] J. Antoniadis et al. (EPTA Collaboration and InPTA Collaboration), Astron. Astrophys. 678, A50 (2023).
- [55] J. Antoniadis et al. (EPTA Collaboration), Astron. Astrophys. 678, A48 (2023).
- [56] J. Antoniadis et al. (EPTA Collaboration and InPTA Collaboration), Astron. Astrophys. 678, A49 (2023).
- [57] J. Antoniadis et al., arXiv:2306.16226.
- [58] J. Antoniadis et al., Astron. Astrophys. **685**, A49 (2024).
- [59] V. Vaskonen and H. Veermäe, Phys. Rev. Lett. **126**, 051303 (2021).
- [60] V. De Luca, G. Franciolini, and A. Riotto, Phys. Rev. Lett. 126, 041303 (2021).
- [61] K. Kohri and T. Terada, Phys. Lett. B 813, 136040 (2021).
- [62] S. Sugiyama, V. Takhistov, E. Vitagliano, A. Kusenko, M. Sasaki, and M. Takada, Phys. Lett. B 814, 136097 (2021).
- [63] K. Inomata, M. Kawasaki, K. Mukaida, and T. T. Yanagida, Phys. Rev. Lett. 126, 131301 (2021).
- [64] V. Atal, A. Sanglas, and N. Triantafyllou, J. Cosmol. Astropart. Phys. 06 022 (2021).
- [65] M. Kawasaki and H. Nakatsuka, J. Cosmol. Astropart. Phys. 05 023 (2021).
- [66] F. Hasegawa and M. Kawasaki, Phys. Rev. D 98, 043514 (2018).
- [67] M. Kawasaki and K. Murai, Phys. Rev. D **100**, 103521 (2019).

- [68] N. Kitajima and F. Takahashi, J. Cosmol. Astropart. Phys. 11 060 (2020).
- [69] T. Shinohara, T. Suyama, and T. Takahashi, Phys. Rev. D 104, 023526 (2021).
- [70] K. Inomata, E. McDonough, and W. Hu, Phys. Rev. D **104**, 123553 (2021).
- [71] O. Ozsoy and Z. Lalak, J. Cosmol. Astropart. Phys. **01** 040 (2021).
- [72] K. Rezazadeh, K. Karami, and P. Karimi, J. Cosmol. Astropart. Phys. 09, 053 (2015).
- [73] S. Unnikrishnan, V. Sahni and A. Toporensky, J. Cosmol. Astropart. Phys. 08, 018 (2012).
- [74] S. Unnikrishnan and V. Sahni, J. Cosmol. Astropart. Phys. 10, 063 (2013).
- [75] S. S. Mishra, V. Sahni, and A. Toporensky, Phys. Rev. D 98, 083538 (2018).
- [76] S. S. Mishra, V. Sahni and A. A. Starobinsky, J. Cosmol. Astropart. Phys. 05, 075 (2021).
- [77] I. Safaei and K. Karami, arXiv:2404.04872.
- [78] J. Garriga, and V. F. Mukhanov, Phys. Lett. B 458, 219 (1999).
- [79] Y. Akrami et al. (Planck Collaboration), Astron. Astrophys. 641, A10 (2020).
- [80] P.A.R. Ade et al. (BICEP/Keck Collaboration), Phys. Rev. Lett. 127, 151301 (2021).
- [81] S. K. Garg and C. Krishnan, J. High Energy Phys. 11, 075 (2019).
- [82] H. Ooguri, E. Palti, G. Shiu and C. Vafa, Phys. Lett. B 788, 180 (2019).
- [83] A. Kehagias and A. Riotto, Fortschr. Phys. **66**, 1800052 (2018).
- [84] K. Inomata and T. Nakama, Phys. Rev. D 99, 043511 (2019).
- [85] K. Inomata, M. Kawasaki, and Y. Tada, Phys. Rev. D 94, 043527 (2016).
- [86] D. Jeong, J. Pradler, J. Chluba, M. Kamionkowski, Phys. Rev. Lett. 113, 061301 (2014).
- [87] T. Nakama, T. Suyama, and J. Yokoyama, Phys. Rev. Lett. 113, 061302 (2014).
- [88] D. J. Fixsen, E. S. Cheng, J. M. Gales, J. C. Mather, R. A. Shafer, and E. L. Wright, Astrophys. J. 473, 576 (1996).
- [89] J. Chluba, A. L. Erickek, and I. Ben-Dayan, Astrophys. J. 758, 76 (2012).
- [90] B. J. Carr, Astrophys. J. **201**, 1 (1975).
- [91] Y. Tada and S. Yokoyama, Phys. Rev. D **100**, 023537 (2019).
- [92] S. Young, C. T. Byrnes, and M. Sasaki, J. Cosmol. Astropart. Phys. **07** 045 (2014).
- [93] I. Musco and J. C. Miller, Class. Quant. Grav. **30**, 145009 (2013).
- [94] T. Harada, C.-M. Yoo, and K. Kohri, Phys. Rev. D 88, 084051 (2013).
- [95] P. D. Serpico, V. Poulin, D. Inman, and K. Kohri, Phys. Rev. Res. 2, 023204 (2020).
- [96] B. J. Kavanagh, D. Gaggero, and G. Bertone, Phys. Rev. D 98, 023536 (2018).
- [97] B. P. Abbott, R. Abbott, T. D. Abbott, S. Abbott, F. Abraham, and K. Acernese et al.,

- Phys. Rev. Lett. 123, 161102 (2019).
- [98] Z. C. Chen and Q. G. Huang, J. Cosmol. Astropart. Phys. 20, 039 (2020).
- [99] C. Boehm, A. Kobakhidze, C. A. J. O'hare, Z. S. C. Picker, and M. Sakellariadou, J. Cosmol. Astropart. Phys. 03, 078 (2021).
- [100] C. Alcock, R. A. Allsman, D. R. Alves, T. S. Axelrod, A. C. Becker, and D. P. Bennett et al., Astrophys. J. Lett. 550, L169 (2001).
- [101] P. Tisserand, L. Le Guillou, C. Afonso, J. N. Albert, J. Andersen, and E. Ansari et al., Astron. Astrophys. 469, 387–404 (2007).
- [102] K. Griest, A. M. Cieplak, and M. J. Lehner, Astrophys. J. 786, 158 (2014).
- [103] M. Oguri, J. M. Diego, N. Kaiser, P. L. Kelly, and T. Broadhurst, Phys. Rev. D 97, 023518 (2018).
- [104] D. Croon, D. McKeen, N. Raj, and Z. Wang, Phys. Rev. D 102, 083021 (2020).
- [105] S. Mittal, A. Ray, G. Kulkarni, and B. Dasgupta, J. Cosmol. Astropart. Phys. 03, 030 (2022).
- [106] B. J. Carr, K. Kohri, Y. Sendouda, and J. Yokoyama, Phys. Rev. D 81, 104019 (2010).
- [107] S. Clark, B. Dutta, Y. Gao, L. E. Strigari, and S. Watson, Phys. Rev. D 95, 083006 (2017).
- [108] B. Dasgupta, R. Laha, and A. Ray, Phys. Rev. Lett. 125, 101101 (2020).
- [109] C. J. Moore, R. H. Cole, and C. P. L. Berry, Class. Quant. Grav. 32, 015014 (2015).
- [110] R. D. Ferdman et al., Class. Quant. Grav. 27, 084014 (2010).
- [111] G. Hobbs et al., Class. Quant. Grav. 27, 084013 (2010).
- [112] M. A. McLaughlin, Class. Quant. Grav. 30, 224008 (2013).
- [113] G. Hobbs, Class. Quant. Grav. **30**, 224007 (2013).
- [114] P. Amaro-Seoane et al. (LISA Collaboration), Phys. Rev. A 96, 012124 (2017).
- [115] K. Danzmann, Class. Quant. Grav. 14, 1399 (1997).
- [116] K. Yagi and N. Seto, Phys. Rev. D 83, 044011 (2011).
- [117] E. Phinney et al., Big Bang Observer mission concept study (2003).
- [118] N. Seto, S. Kawamura, and T. Nakamura, Phys. Rev. Lett. 87, 221103 (2001).
- [119] K. Kohri and T. Terada, Phys. Rev. D 97, 123532 (2018).
- [120] Y. Lu, Y. Gong, Z. Yi and F. Zhang, J. Cosmol. Astropart. Phys. 12, 031 (2019).
- [121] W. T. Xu, J. Liu, T. J. Gao, and Z. K. Guo, Phys. Rev. D 101, 023505 (2020).
- [122] S. Kuroyanagi, T. Chiba, and T. Takahashi, J. Cosmol. Astropart. Phys. 11, 038 (2018).
- [123] C. Yuan, Z. C. Chen, and Q. G. Huang, Phys. Rev. D 101, 043019 (2020).

- [124] R-G. Cai, S. Pi, and M. Sasaki, Phys. Rev. D ${\bf 102},\,083528$ (2020).
- [125] C. Yuan, D. S. Meng, and Q. G. Huang, J. Cosmol. Astropart. Phys. 12, 036 (2023).